Section S1 Experimental.

1. Materials

Sodium nitroprusside ($C_5H_4FeN_6Na_2O_3$, 99.98%), salicylic acid ($C_7H_6O_3$, 99.5%), and sodium hypochlorite (NaClO, 6-14% active chlorine basis) were purchased in Ron Reagent. Trisodium citrate ($C_6H_5O_7Na_3 \cdot H_2O$, ≥99.5%) was purchased from Tianjin Damao Chemical Trading Co., Ltd. NaOH (96%) were purchased from Tianjin Kermel Chemical Reagent Co., Ltd. Acetone (CH_3COCH_3, 99.5%), ethylene glycol ($HOCH_2CH_2OH$), concentrated hydrochloric acid (36.0-38.0%) were obtained from Tianjin Wind Ship Chemical Reagent Co., Ltd. Anhydrous sodium sulfate (Na_2SO_4, 99%), ascorbic acid (AA, > 99.0%), chloric acid (Au 23.5 ~ 23.8% in dilute HCl), potassium bromide (KBr, photographic primary), Ammonium chloride (NH_4Cl, 99.99%) were obtained from Aladdin. Anhydrous ethanol (CH_3CH_2OH, 99.7%) was purchased from Shandong Bocheng Chemical Co., Ltd. Polyethylene pyrrolidone (PVP, average M.W. = 130,000, 99%) was from Shanghai Yuanye Bio-Technology Co., Ltd. Anhydrous copper sulfate ($CuSO_4$) was purchased from Shanghai Meryer Biochemical Technology Co., Ltd. Paradimethylaminobenzaldehyde ($C_9H_{11}NO$) was obtained from was obtained from Maclin. Hydrazine hydrate (N_2H_4, 5% HCl) was obtained from Guobiao (Beijing) Testing and Certification, Co., Ltd. All chemical reagents were used without further purification.

Transmission electron microscopy (TEM) imaging was performed on a Philips Tecnai F20 system at 200 kV to observe the morphology and quantitatively and qualitatively analyze the elements by EDS mapping. Powder X-ray diffraction (XRD) patterns were recorded on a Bruker GADDS XRD diffractometer with Cu Kα radiation to obtain the structures of composites. The chemical composition and bonding characteristics were analyzed by X-ray photoelectron spectroscopy (XPS) of PHI Quantera under monochromatic Mg X-ray radiation source. The composition analysis of the materials was also performed using Aglient 7800 model ICP-OES. ENRR tests were conducted using a CHI760E electrochemical workstation and

Solartron, Modulab XM, UK.

2. Synthesis

NP-AuCu alloy materials were prepared by a facile wet-chemical method. In general, the synthesis of NP-AuCu alloys utilized polyvinylpyrrolidone as the surfactant. In the ethylene glycol system, copper sulfate was used as the copper source, ascorbic acid reduced the copper element to Cu (0) , and then $HAuCl_4$ was used as the gold source, potassium bromide was used as the reducing agent for reducing gold to couple the alloy metals.

First, 50 mg of polyvinylpyrrolidone (PVP) and 450 mg of ascorbic acid (AA) were mixed evenly in round bottom flask. Then followed by adding 8 mL of ethylene glycol (EG), the reaction was stirred thoroughly for 10 minutes. The round-bottom flask was then moved into an oil bath and heated to 85 ^{o}C. Two-mL $CuSO_4$ solution (3.6 mg) was added to the flask. The color of the solution changed from colorless to pink. After heating the solution at 85 ℃ for 30 minutes, 2-mL KBr solution (375 mg) and 2-mL $HAuCl_4$ solution (19 mg) were added. The solution changed from pink to purple, indicating that Au (0) was generated under the action of reducing agent. The reaction was kept for 90 minutes to couple Au with Cu to generate NP-AuCu alloy materials. After finally cooling the solution to room temperature, the products were collected by centrifugation and washing with ethanol and acetone to remove the precursor and by-products, and dried under vacuum for 6 hours.

3. eNRR measurement

5-mg NP-AuCu alloy materials were dispersed in 1 mL of ethanol. NP-AuCu catalyst solution (3 μL, 5 mg/mL) was dropped on the surface of the polished glass carbon electrode and naturally dried at room temperature. ENRR measurements were performed on an electrochemical workstation using a three-electrode system. NP-AuCu alloy nanomaterials were used as the working electrode, Ag/AgCl as the reference electrode, and Pt sheet as the counter electrode for electrolysis in an electrolytic cell with 0.1 $mol \cdot L^{-1}$ Na_2SO_4 electrolyte. Before each electrochemical test,

N_2 was continuously fed into the electrolyte for at least 1h. All given potentials were converted to reversible hydrogen electrode potential by E(vs RHE) = E(vs Ag/AgCl) + 0.059 pH + 0.197 V. Electrochemical test was performed for 2 h at the applied potentials of -0.75 V, -0.80 V, -0.85 V, -0.90 V, -0.95 V, and -0.10 V vs. RHE. The constant and stable access of N_2 is maintained during the electrolysis process.

4. Detection of ammonia

Ammonia in the electrolyte was quantified after 2-h electrolysis by indophenol blue method. Firstly, the color reagent system were prepared. Solution A: 1 M NaOH solution (containing 5% salicylic acid and 5% sodium citrate); solution B: 0.05 M NaClO solution; solution C: 1 wt% $C_5FeN_6Na_2O$ (sodium nitroferricyanide) aqueous solution. 2 mL of electrolyte was mixed with 2 mL solution A, 1 mL solution B and 0.2 mL solution C evenly, and the reaction was kept for 2 h at room temperature. The absorbance at 655 nm was recorded by using a UV-Vis absorption spectrometer. Next, NH_4Cl standard solution with a series of different concentrations was configured for UV-Vis tests and the standard curve of indophenol blue method was drawn to detect ammonia. The ammonia concentration in the electrolyte was calculated by the linear equations.

5. Detection of hydrazine

The by-product N_2H_4 in the electrolyte was quantified after 2-h electrolysis by Watt-Chrisp method. Firstly, the color reagent system was prepared. P-dimethylaminated benzaldehyde (5.99 mg) was dissolved in a mixture of absolute ethanol (300 mL) and concentrated hydrochloric acid (30 mL). 5 mL of chromogen was mixed with 5 mL of electrolyte and kept at room temperature for 20 min. The absorbance at 455 nm was recorded by using a UV-Vis absorption spectrometer. Then, a series of concentrations of N_2H_4 standard solution was tested by UV-Vis to established the standard curve of N_2H_4. The hydrazine concentration in the electrolyte was calculated by the linear equations.

6. Calculation of ammonia yield rate and faradaic efficiency

The performance of eNRR catalysts mainly depends on their high catalytic activity, high selectivity and excellent stability. The high catalytic activity can be measured by the Faradaic efficiency and the ammonia production rate. Faradaic efficiency (*FE*) refers to the ratio of the charge consumed in the electrocatalytic ammonia synthesis to the total charge passing through the electrode, which can be calculated according to the following equation:

$$FE = \frac{3 \times F \times C_{NH_3} \times V}{17 \times Q}$$

The ammonia production rate can be calculated by using the following equation:

$$v_{NH3} = \frac{C_{NH_3} \times V}{t \times A_{cat.}}$$

where F is Faraday's constant, C_{NH3} is the ammonia concentration determined by indophenol blue method, V is the electrolyte volume of eNRR, Q is the quantity of applied electricity, t is the time of electrochemical reaction, and $A_{cat.}$ is the area covered by the catalyst.

Section S2 Characterization of NP-AuCu, AuNPs and CuNPs.

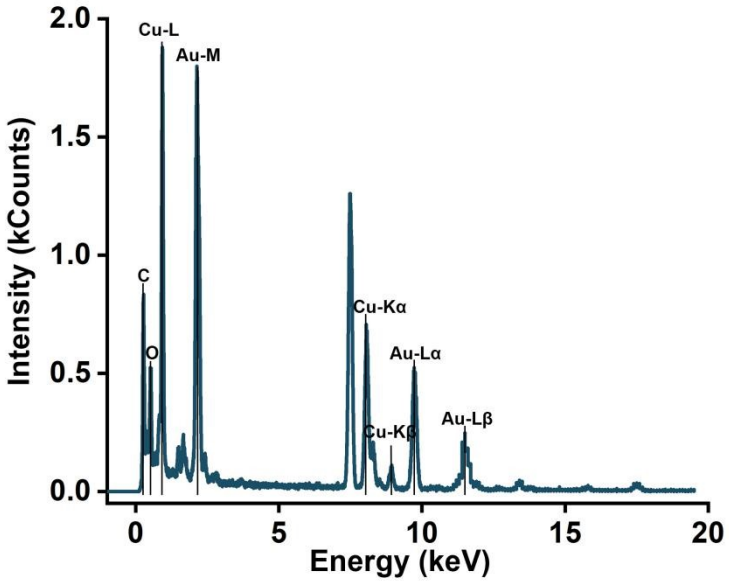

Figure S1. EDS elemental spectrum corresponding to the elemental mapping in Figure 1. EDS signals of Au and Cu are acquired from the peaks at 2.1, 9.8, 11.5, 0.9, 8.1 and 8.9 keV, assigned to Au-M, Au-Lα, Au-Lβ, Cu-L, Cu-Kα and Cu-Kβ, respectively.

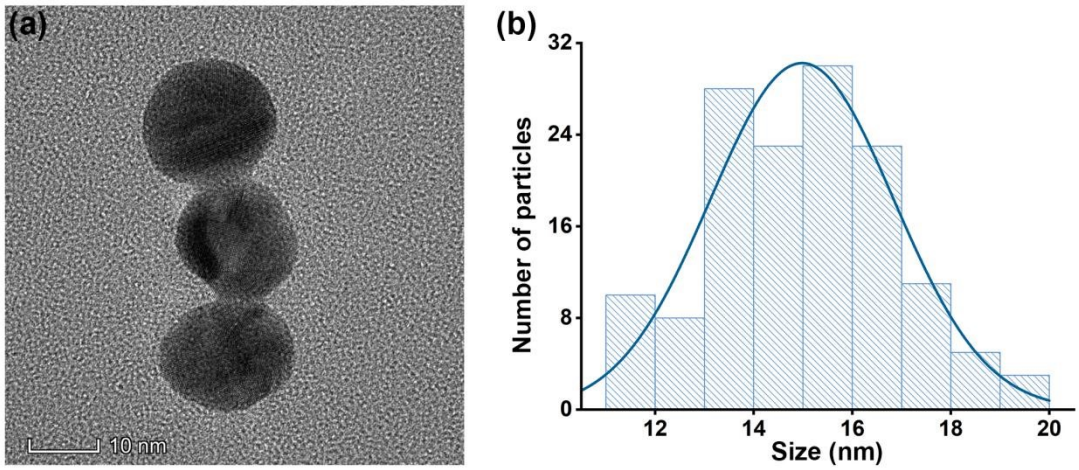

Figure S2. (a) Morphological characterization in the AuNPs in the TEM image. (b) Size distribution diagram of particle size for corresponding AuNPs.

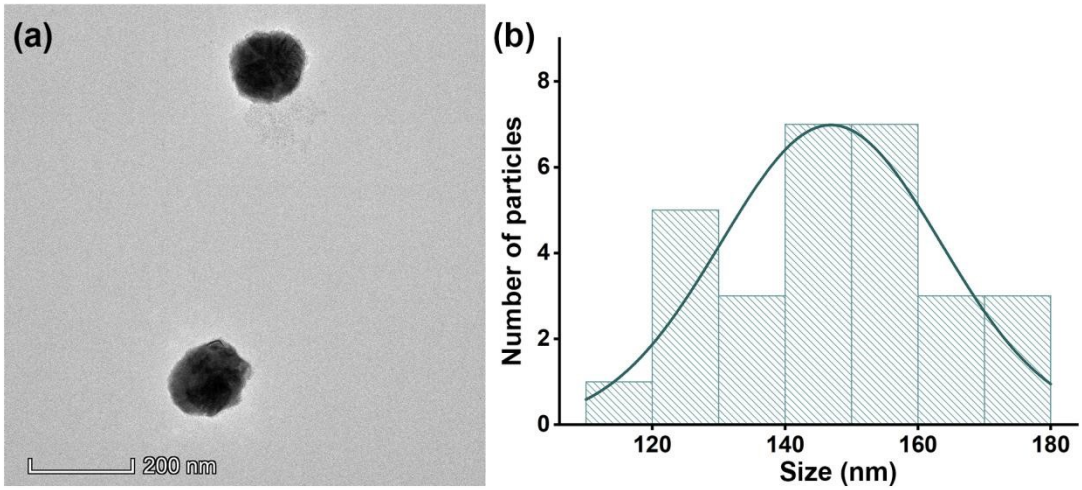

Figure S3. (a) Morphological characterization in the CuNPs in the TEM image. (b) Size distribution diagram of particle size for corresponding CuNPs.

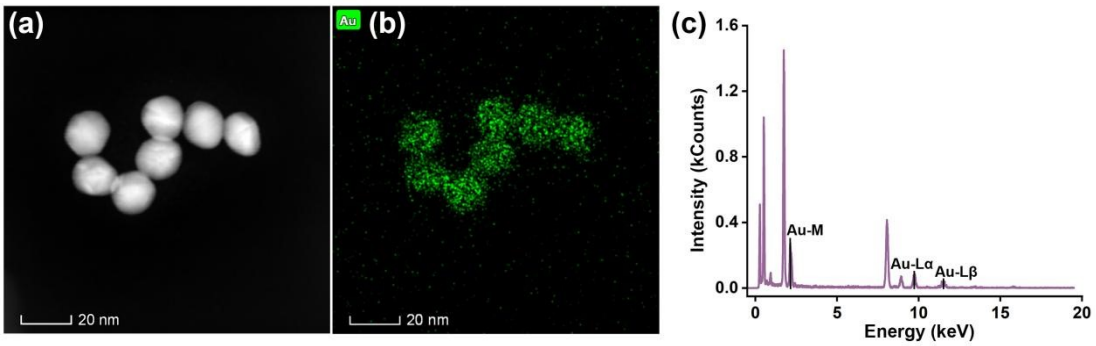

Figure S4. EDS elemental mapping of (a) the AuNPs, indicating (b) Au formation and (c) the corresponding elemental spectrum.

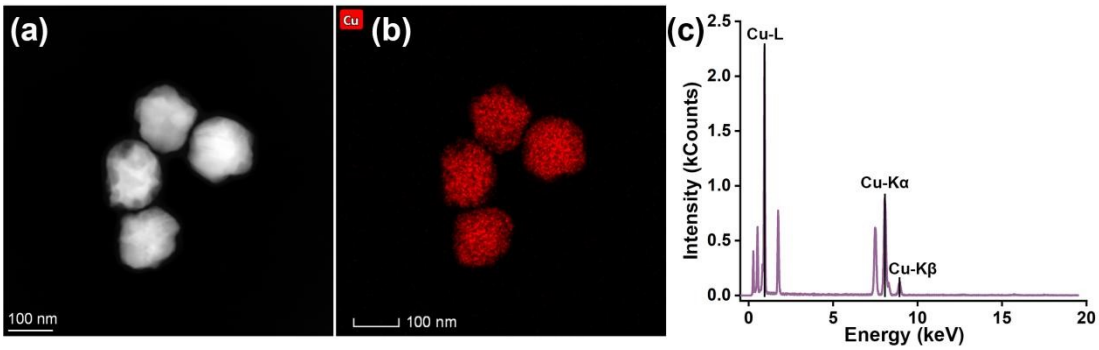

Figure S5. EDS elemental mapping of (a) the CuNPs, indicating (b) Cu and (c) the corresponding elemental spectrum.

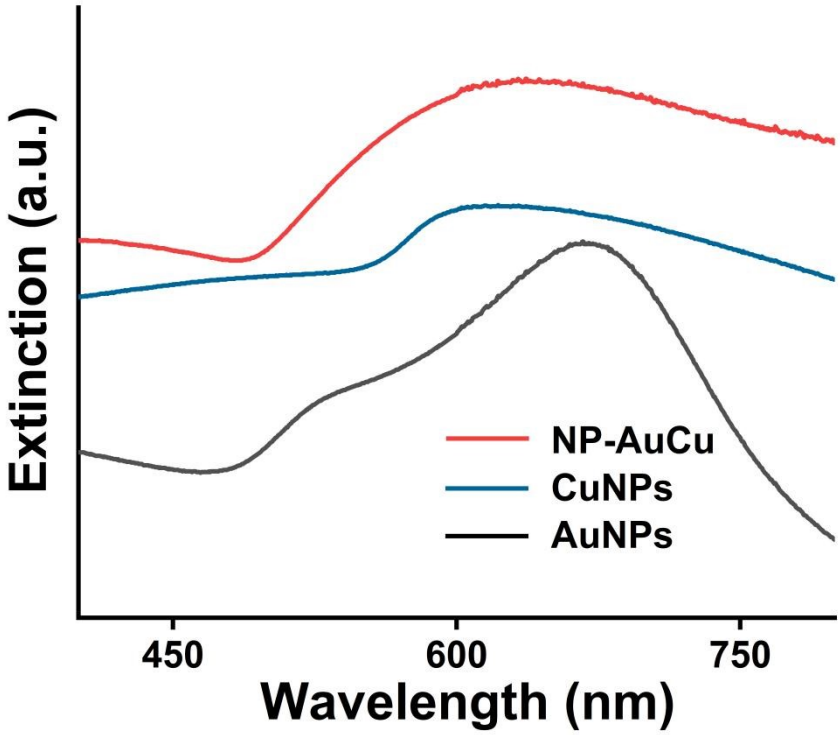

Figure S6. UV-vis absorption spectra of NP-AuCu, AuNPs and CuNPs.

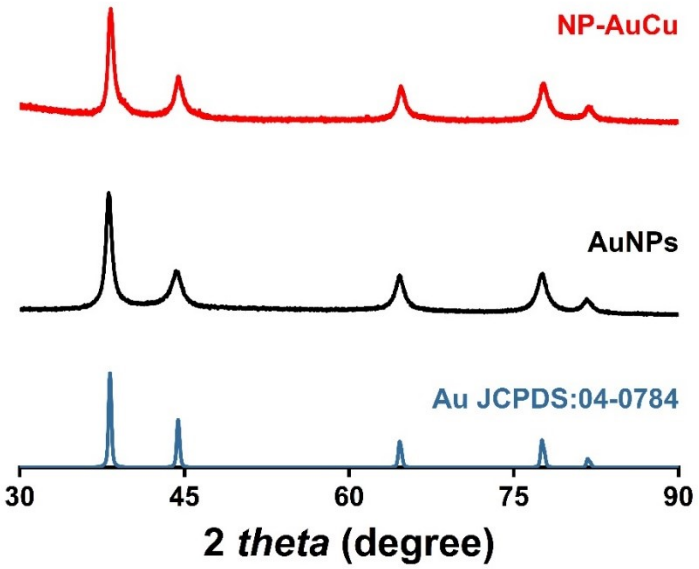

Figure S7. XRD patterns of NP-AuCu and AuNPs. XRD spectrum of NP-AuCu shows five typical diffraction peaks corresponding to the lattice planes of the face centred cubic (fcc) crystalline Au (JCPDS, card No. 04-0784). In contrast with AuNPs, each peak position of NP- AuCu is shifted to higher degree, showing the formation of alloy structures.

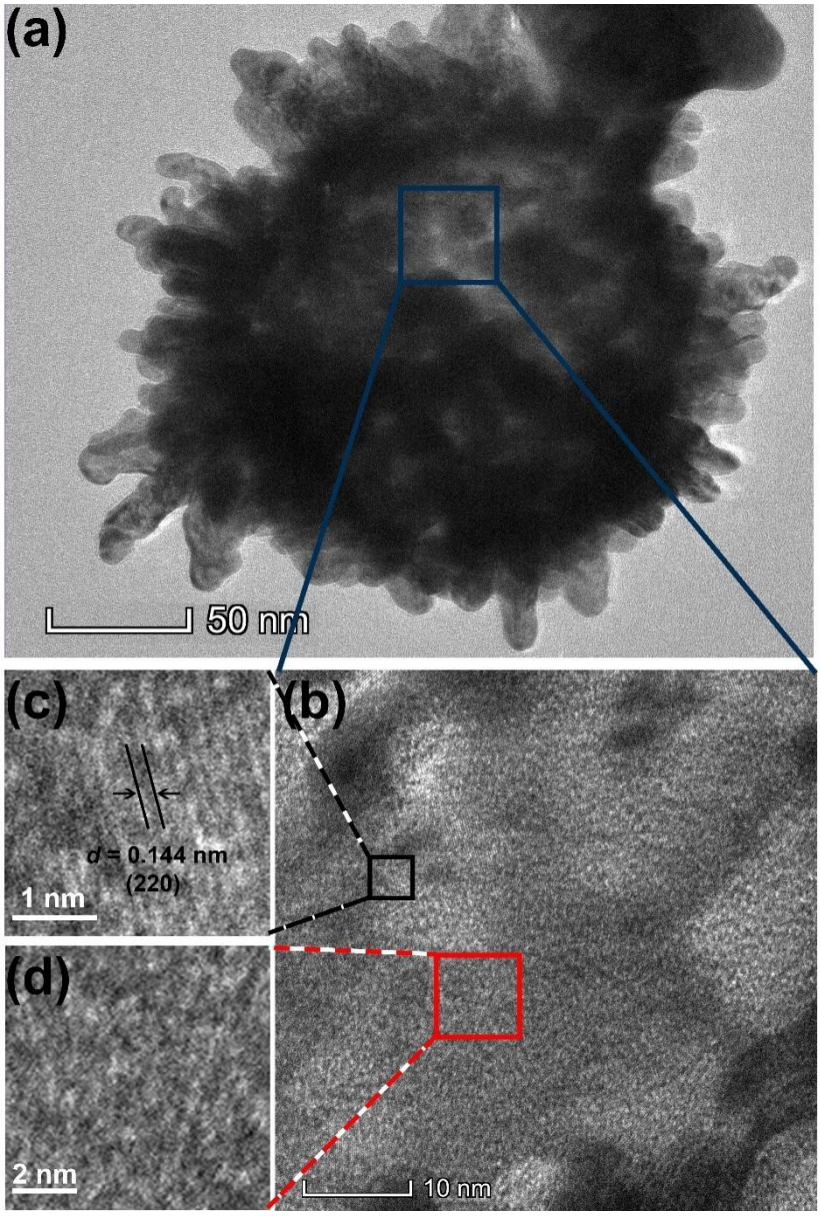

Figure S8. (a) TEM image of NP-AuCu and (b-d) high-resolution TEM image in the square area. The lattice structure of Au shows plane spacing of 0.144 nm, which is indexed to the (220) lattice plane.

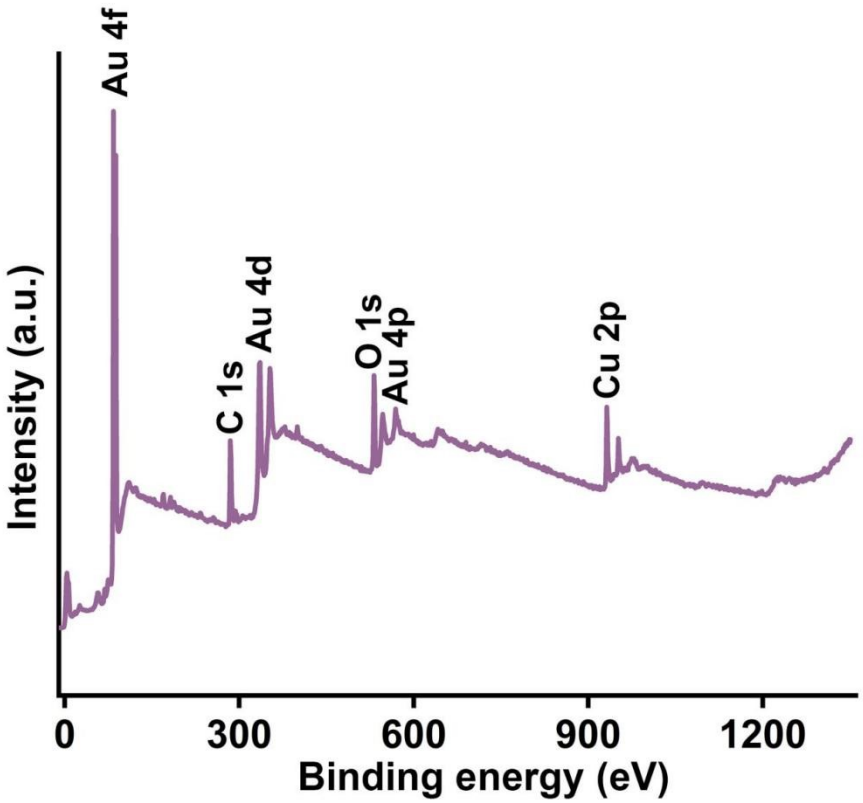

Figure S9. Surface analysis of the NP-AuCu was carried out using X-ray photoelectron spectroscopy. Au 4*f* peak is at 83.9 eV, C 1*s* peak is at 284.8 eV and Cu 2*p* peak is at 932.0 eV.

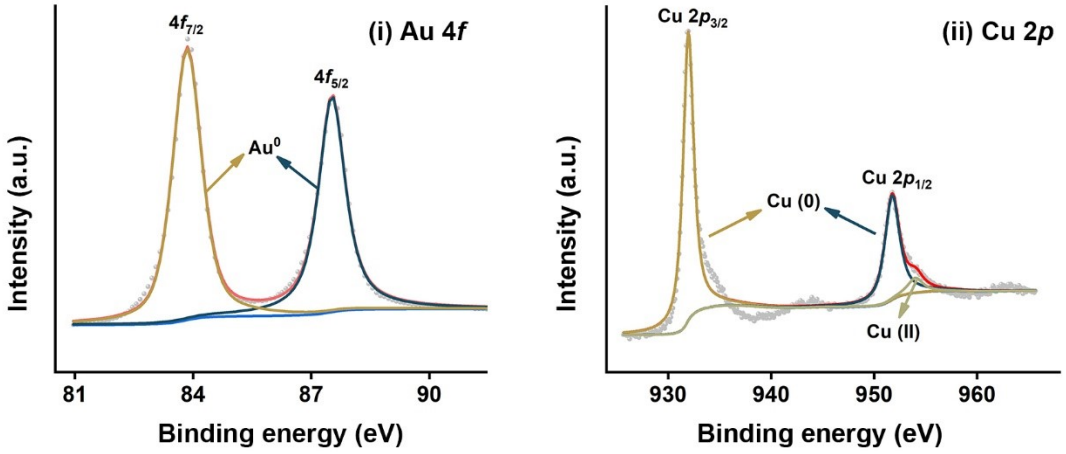

Figure S10. XPS at (i) Au 4*f* and (ii) Cu 2*p* binding energy windows. Au and Cu are further proved to coexist dominantly in their metallic valence states.

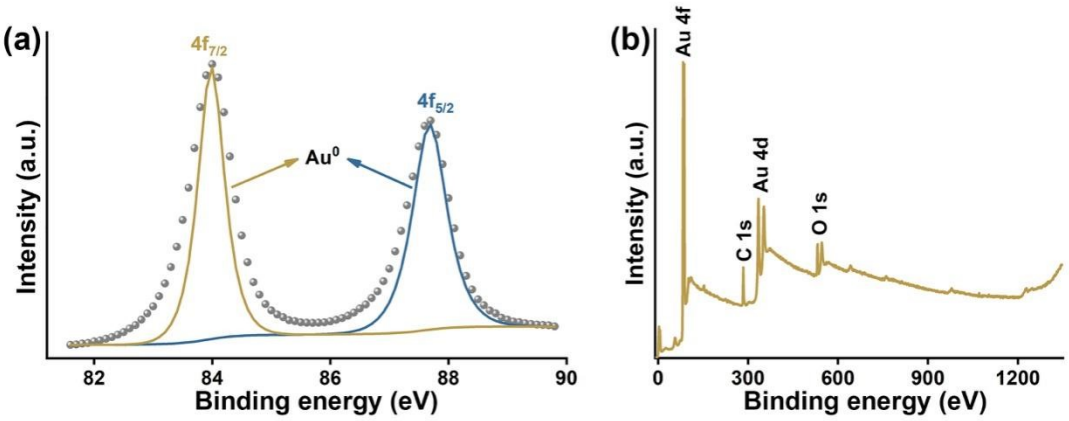

Figure S11. XPS at (a) Au 4*f* binding energy windows (87.7 eV, 84.0 eV). (b) Complete high-resolution scan for AuNPs.

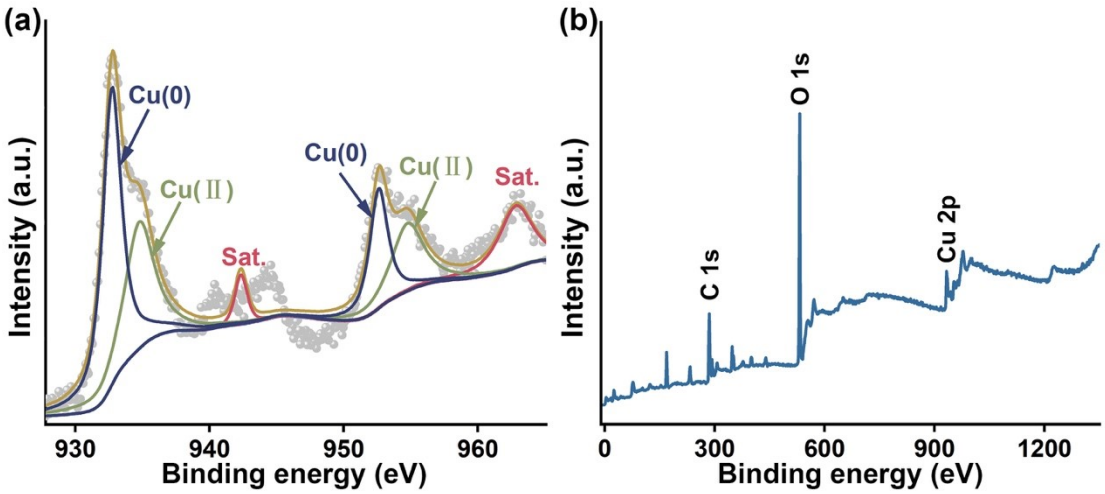

Figure S12. XPS at (a) Cu binding energy windows. (b) Complete high-resolution scan for CuNPs. The coexistence of Cu(0) and Cu(II) in CuNPs is evidenced by a shoulder observed on the main peak at 932.8 eV, which is assigned to Cu(0) species. The higher binding energy (BE) of Cu $2p_{3/2}$ peak at 934.9 eV and its shakeup satellites are due to Cu(II). The other Cu(0) $2p$ peak is at 952.7 eV.

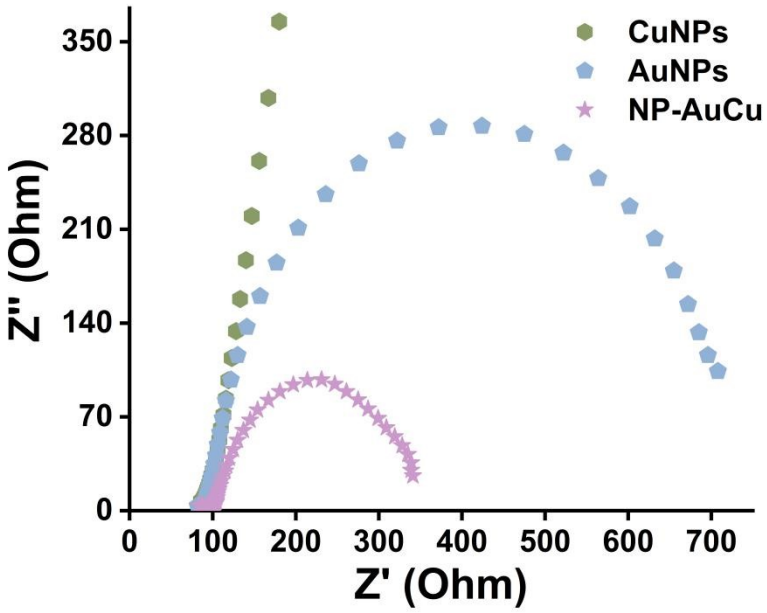

Figure S13. Electrochemical impedance spectroscopy of NP-AuCu, AuNPs and CuNPs.

Section S3 Electrocatalysis

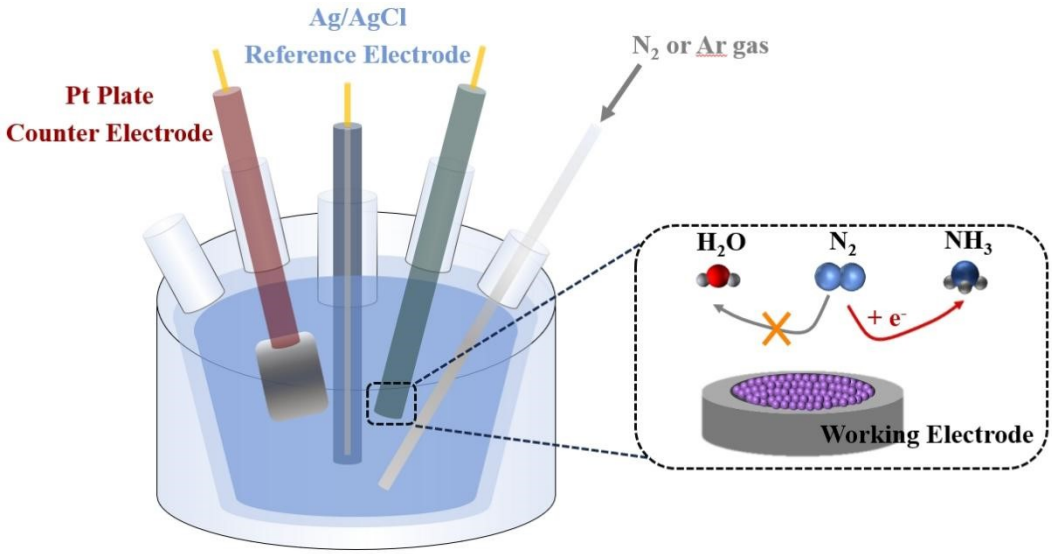

Figure S14. Experimental setup of eNRR. A three-electrode system comprising Pt plate counter electrode, Ag/AgCl reference electrode, and NP-AuCu working electrode was used to conduct the reactions at precisely-controllable voltages, with 0.1 M Na_2SO_4 aqueous solution as the electrolyte.

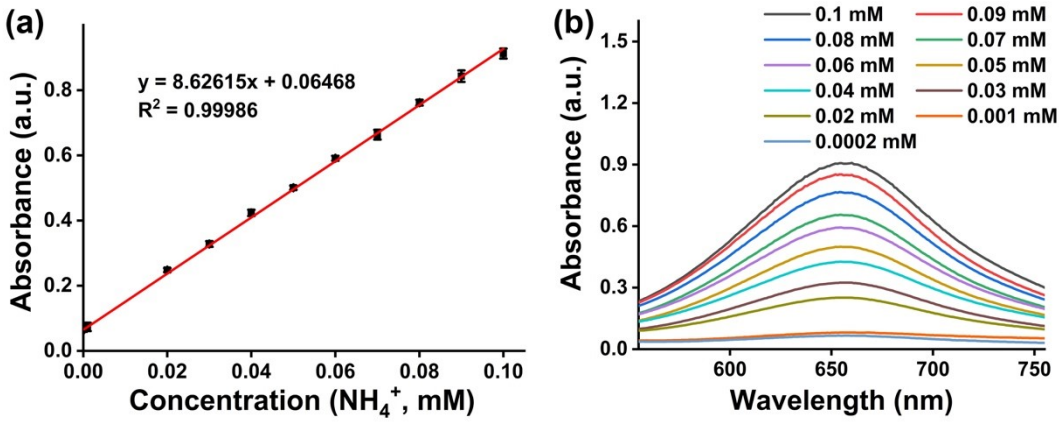

Figure S15. Calibration of the indophenol blue method for subsequent ammonia quantification. (a) Linear correlation of the absorbance intensity to NH_4^+ concentration (inset shows the formation of indophenol blue with different NH_4^+ concentrations). (b) Absorbance spectra of indophenol blue in NH_4^+ solutions at various concentrations.

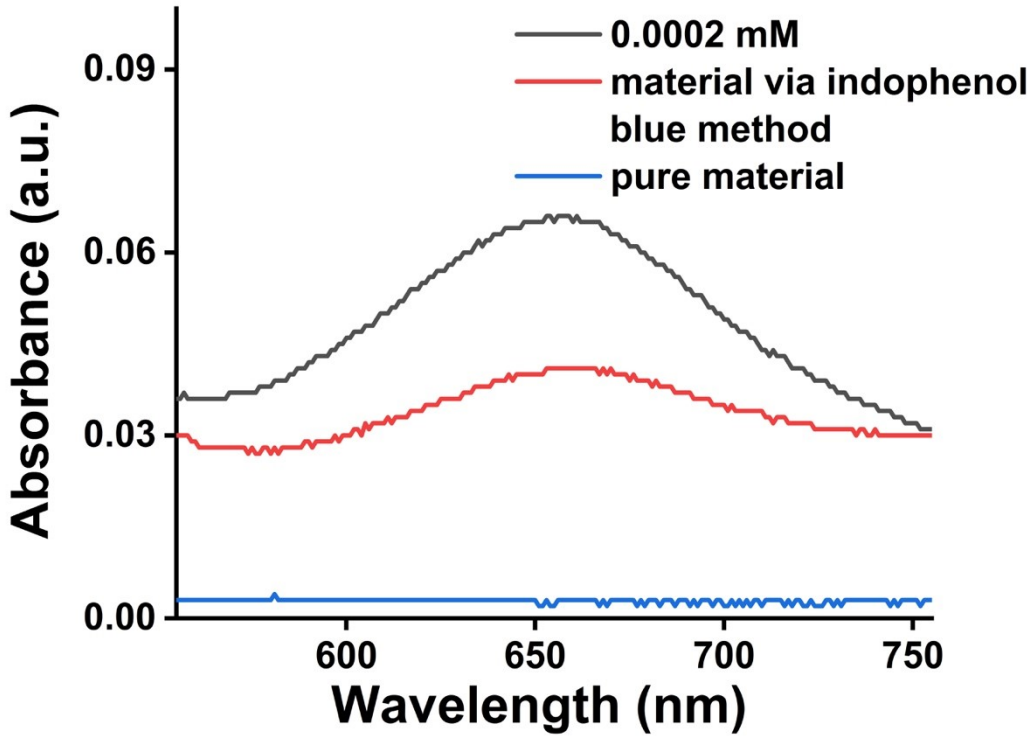

Figure S16. Comparison on UV-vis spectra of NP-AuCu dispersed solution and 0.0002 mM NH_4^+ standard solution via indophenol blue method, as well as the pure NP-AuCu dispersion of the same concentration without indophenol blue test to exclude the possible ammonia contamination.

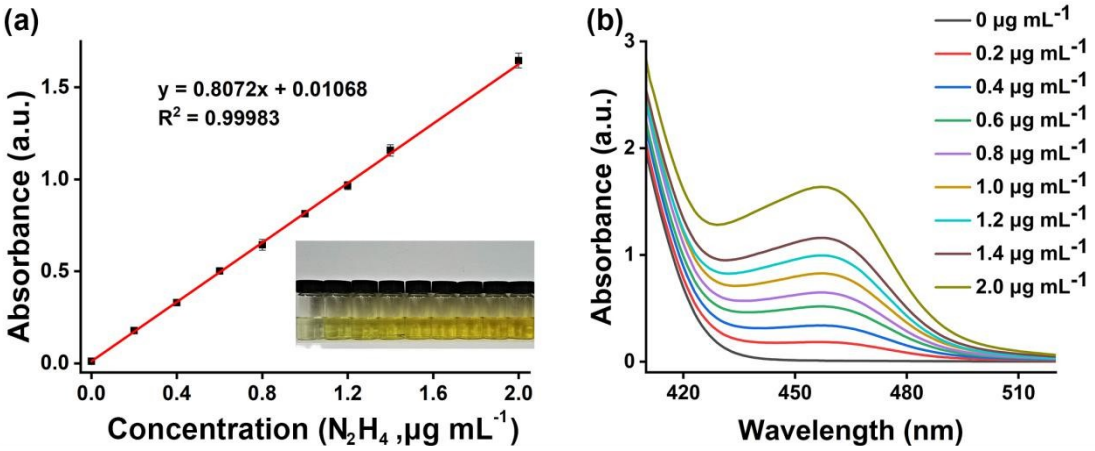

Figure S17. Calibration of the estimation method for subsequent hydrazine quantification. (a) Calibration curve used for calculation of N_2H_4 concentration. (b) Absorbance spectra of N_2H_4 solutions with various concentrations after incubated for 20 minutes at room temperature.

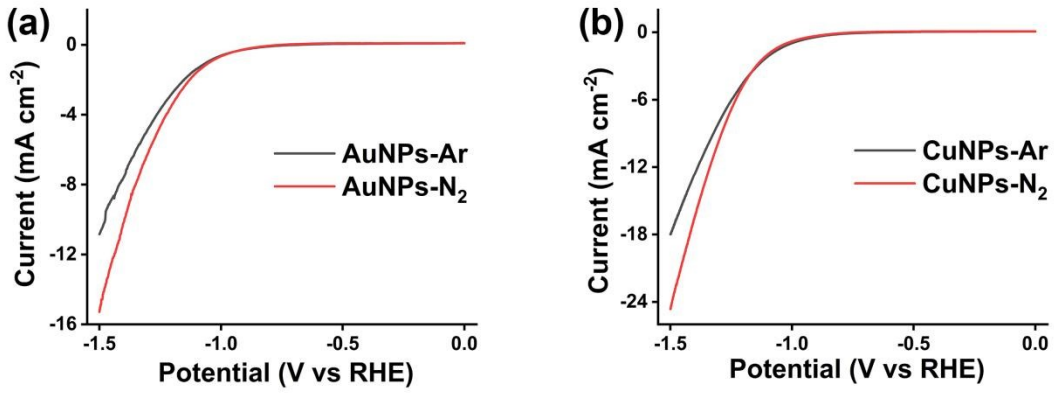

Figure S18. Linear sweep voltammetry measurements in the Ar- or N_2-saturated environments in 0.1 M Na_2SO_4 aqueous solution under ambient conditions, using the (a) AuNPs and (b) CuNPs functionalized electrode.

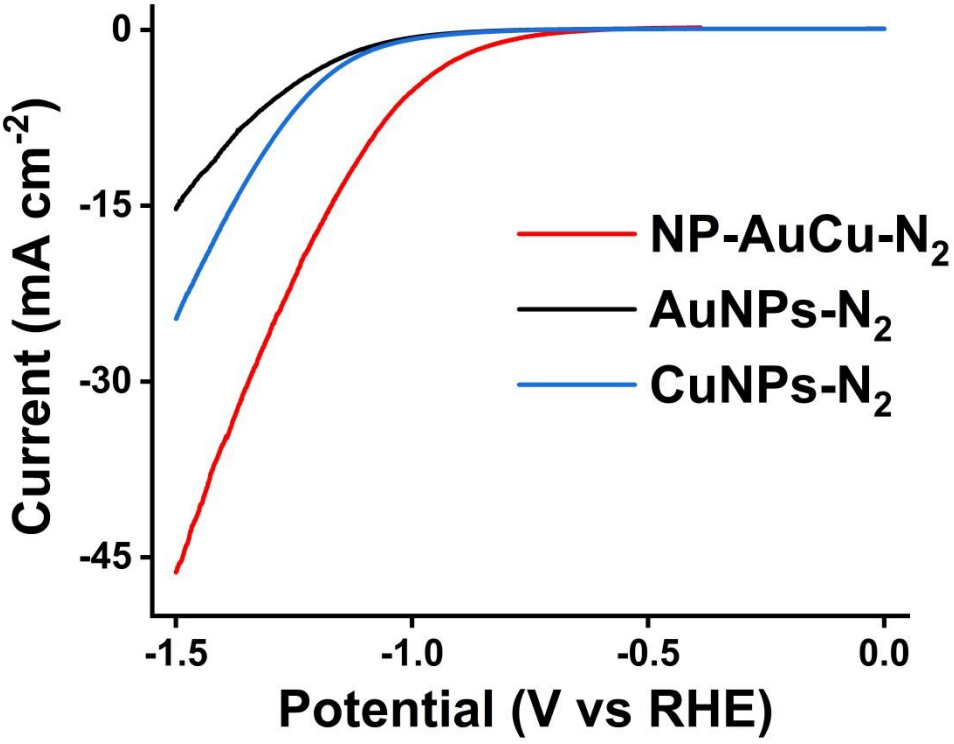

Figure S19. Linear sweep voltammetry measurements in the N_2-saturated environments, using the NP-AuCu, AuNPs and CuNPs functionalized electrodes.

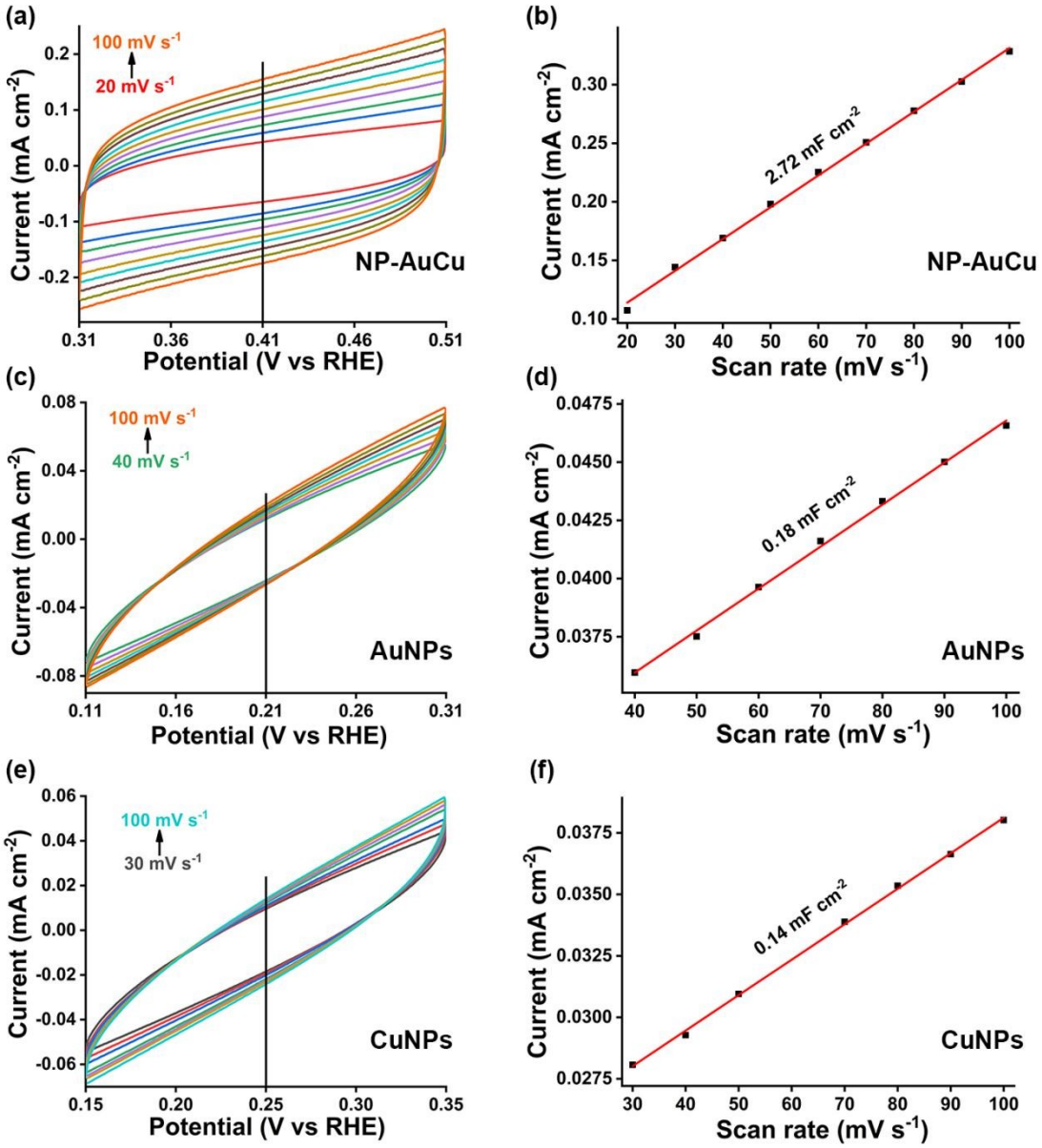

Figure S20. Cyclic voltammetry tests for synthesized (a) NP-AuCu, (c) AuNPs and (e) CuNPs, and (b), (d), (f) charging current density differences plotted against scan rates, respectively.

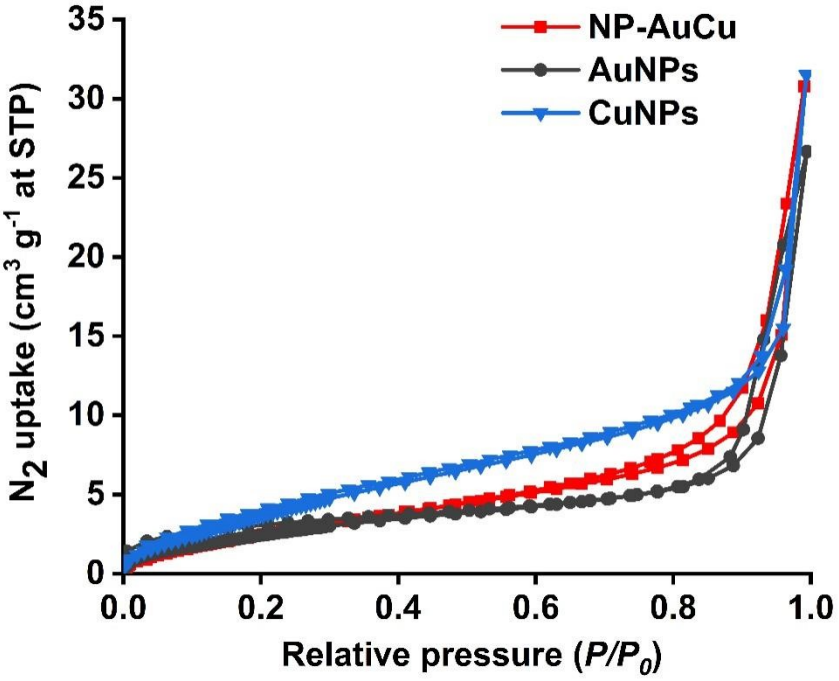

Figure S21. Nitrogen adsorption and desorption isotherms for NP-AuCu, AuNPs and CuNPs. The BET surface area is 11.64 m^2/g.

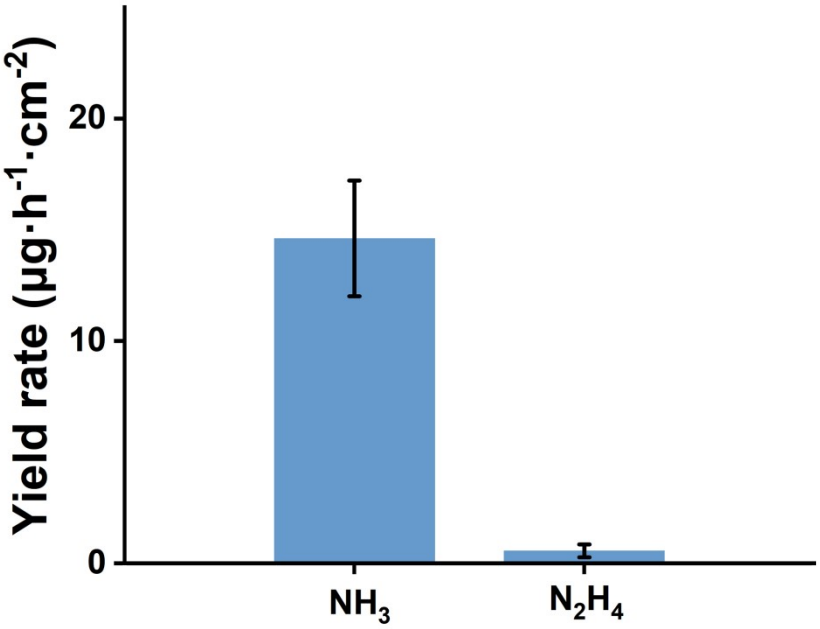

Figure S22. Yield rate for ammonia and hydrazine generated during the eNRR at -0.8 V vs. RHE.

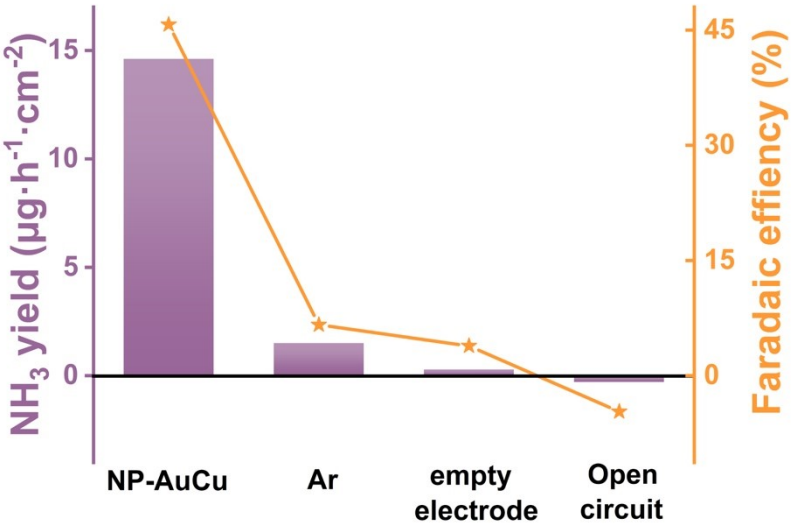

Figure S23. Faradaic efficiency and NH_3 yield comparison under different conditions.

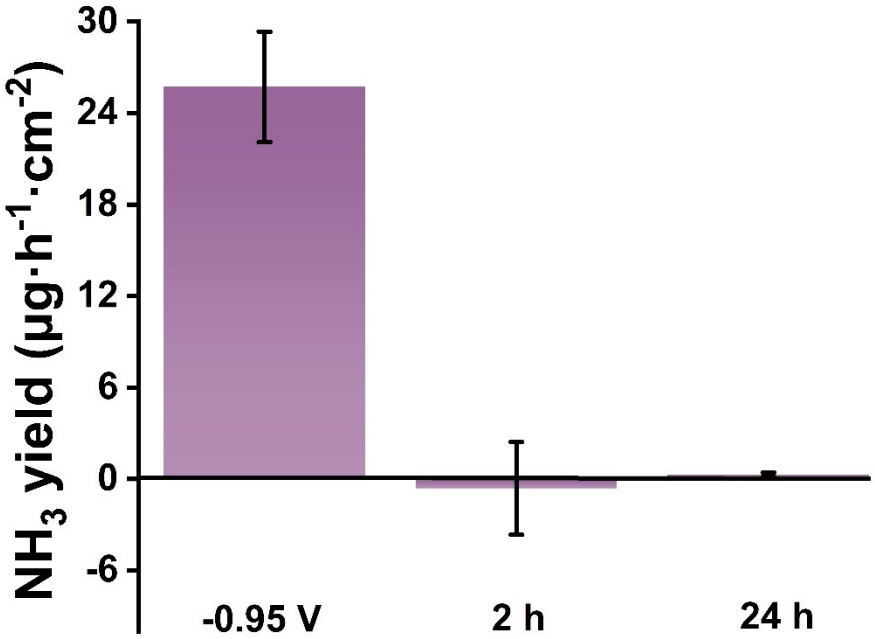

Figure S24. Comparison of ammonia yield under the potential of -0.95 V vs. RHE for 2 hours and without potential applied for 2 and 24 hours.

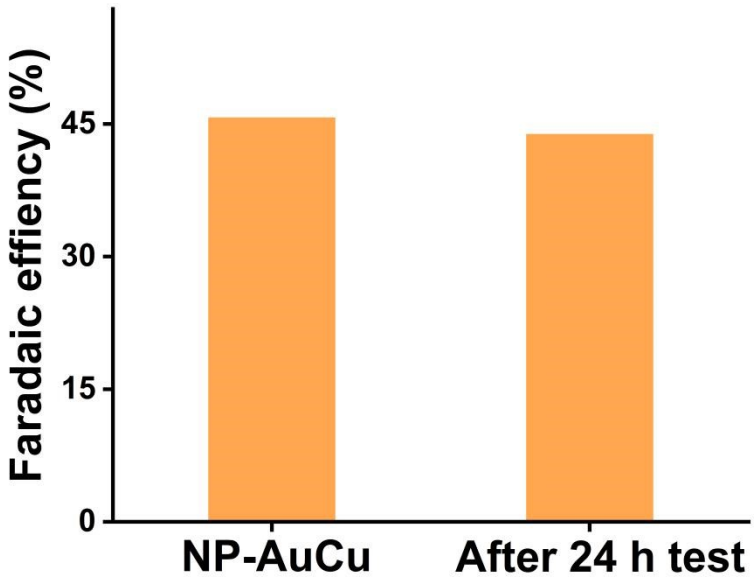

Figure S25. Comparison of Faradaic efficiency before and after 24-h of electrolysis.

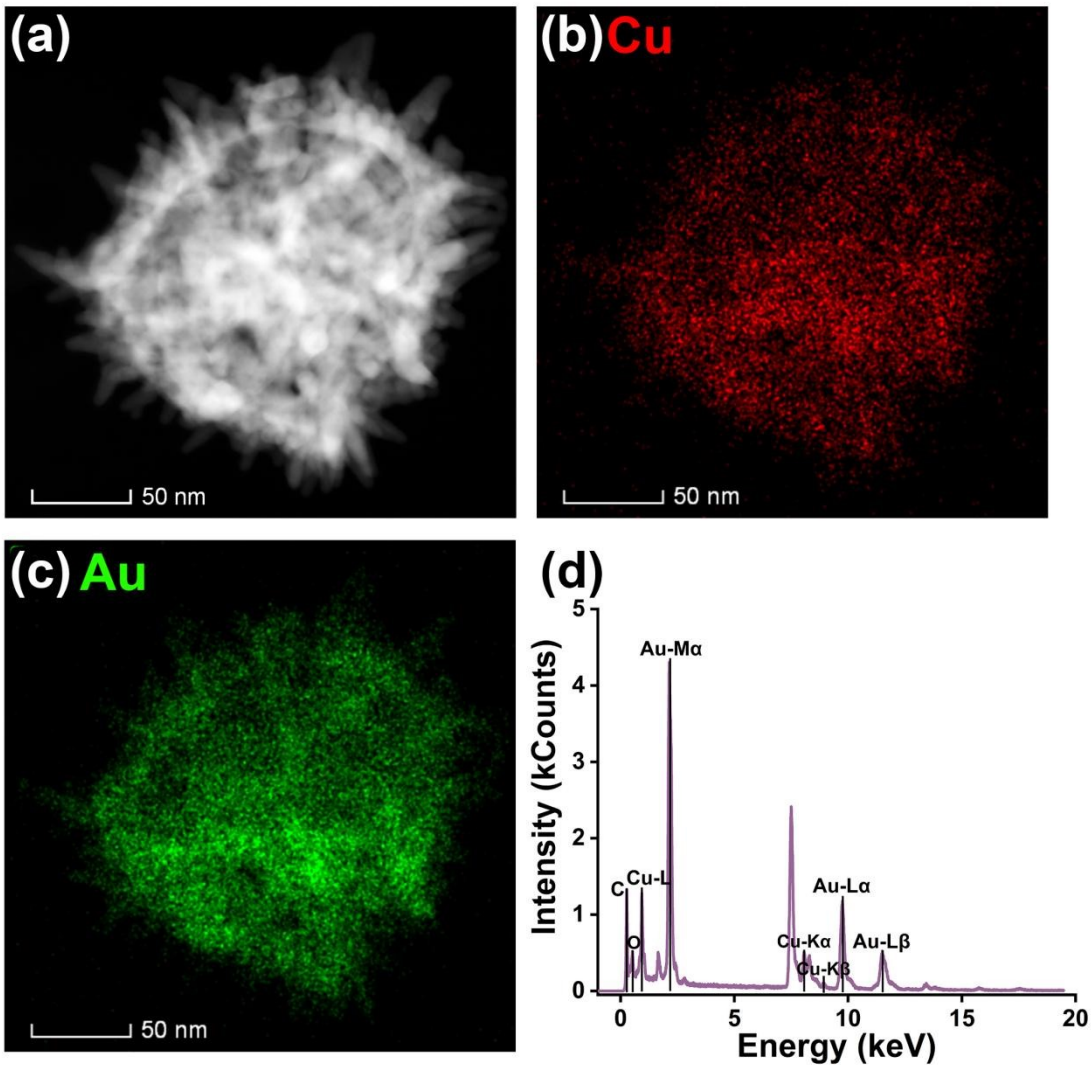

Figure S26. (a) NP-AuCu morphology after 2-h electrolysis in the HAADF-STEM image. EDS elemental mapping of NP-AuCu, indicating (b) Cu and (c) Au , and (d) the corresponding elemental spectrum.

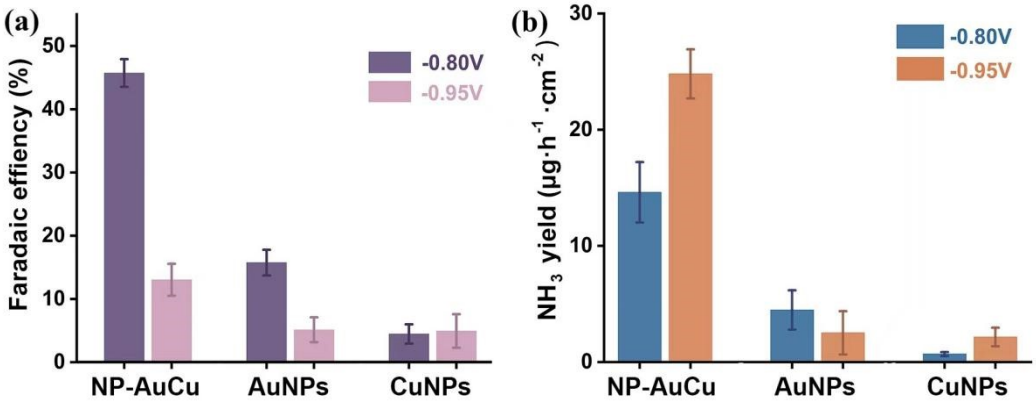

Figure S27. Comparison of the (a) Faradaic efficiency and (d) NH_3 yield of NP-AuCu, AuNPs and CuNPs. Ammonia yield of NP-AuCu is 25.72 $\mu g \cdot h^{-1} \cdot cm^{-2}$ at −0.80 V vs. RHE and 14.61 $\mu g \cdot h^{-1} \cdot cm^{-2}$ at −0.95 V vs. RHE. Faradaic efficiency is 13.04% at −0.80 V vs. RHE and 45.73% at −0.95 V vs. RHE.

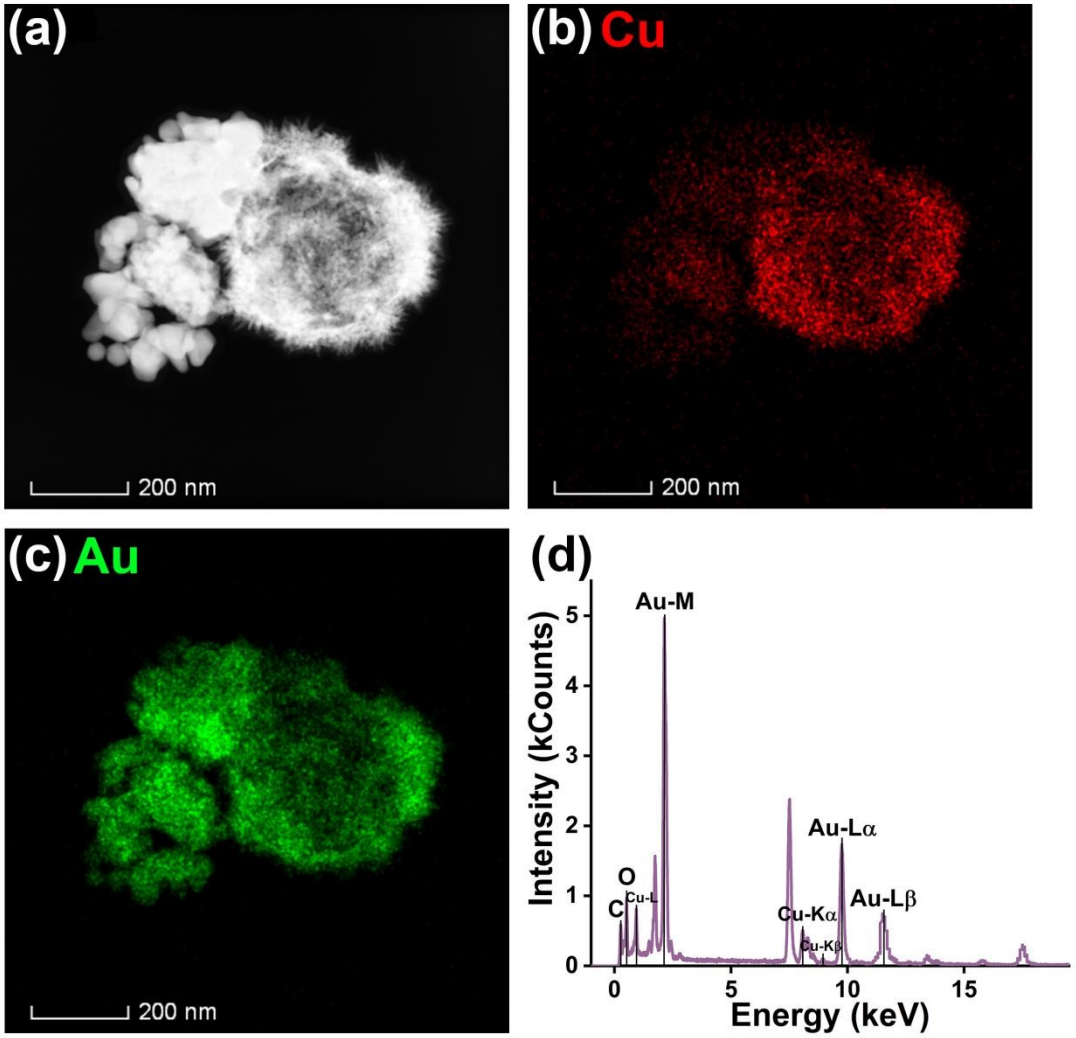

Figure S28. (a) NP-AuCu-2:1 morphology features in the HAADF-STEM image. EDS elemental mapping of NP-AuCu-2:1, indicating (b) Cu and (c) Au , and (d) the corresponding elemental spectrum. The Au:Cu atomic ratio of NP-AuCu-2:1 is 76:24.

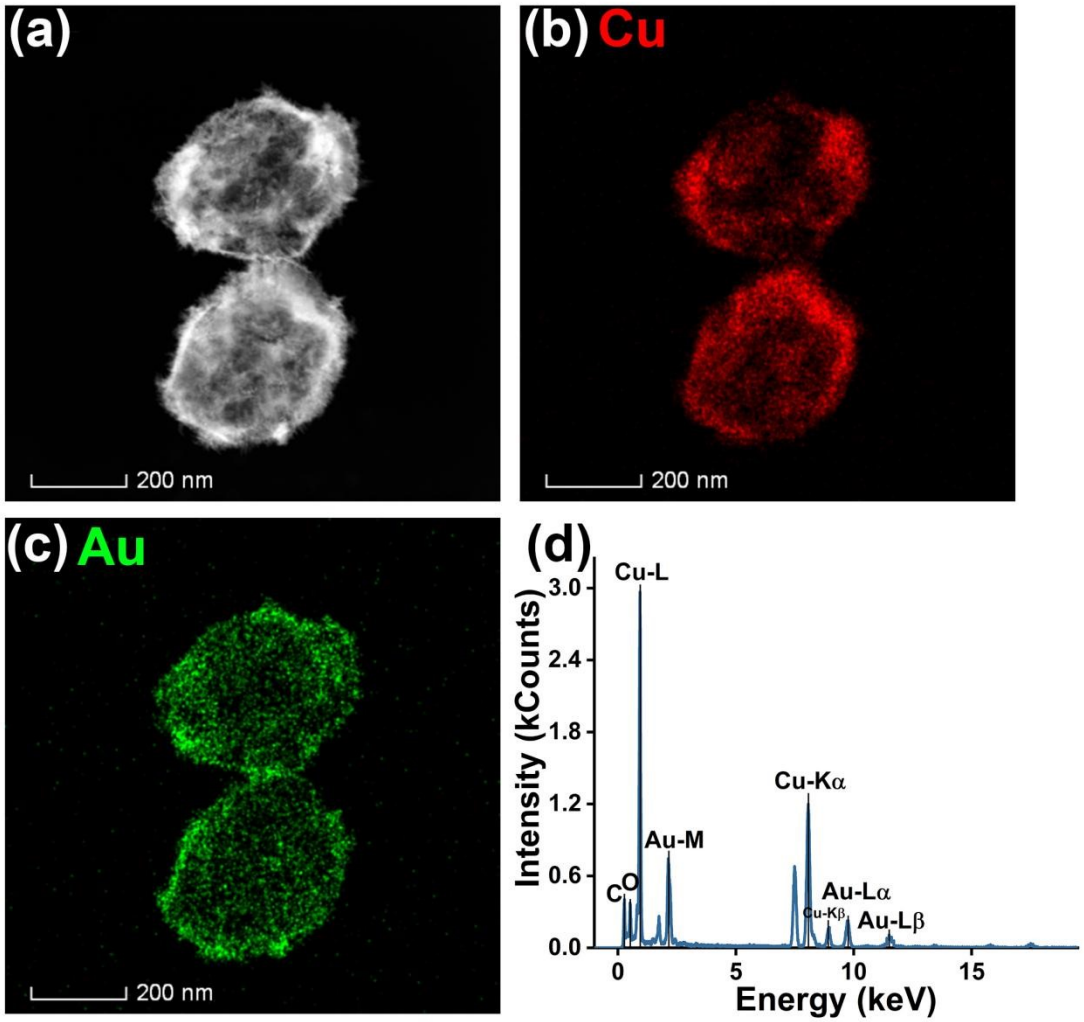

Figure S29. (a) NP-AuCu-1:4 morphology features in the HAADF-STEM image. EDS elemental mapping of NP-AuCu-1:4, indicating (b) Cu and (c) Au , and (d) the corresponding elemental spectrum. The Au:Cu atomic ratio of NP-AuCu-1:4 is 14:86.

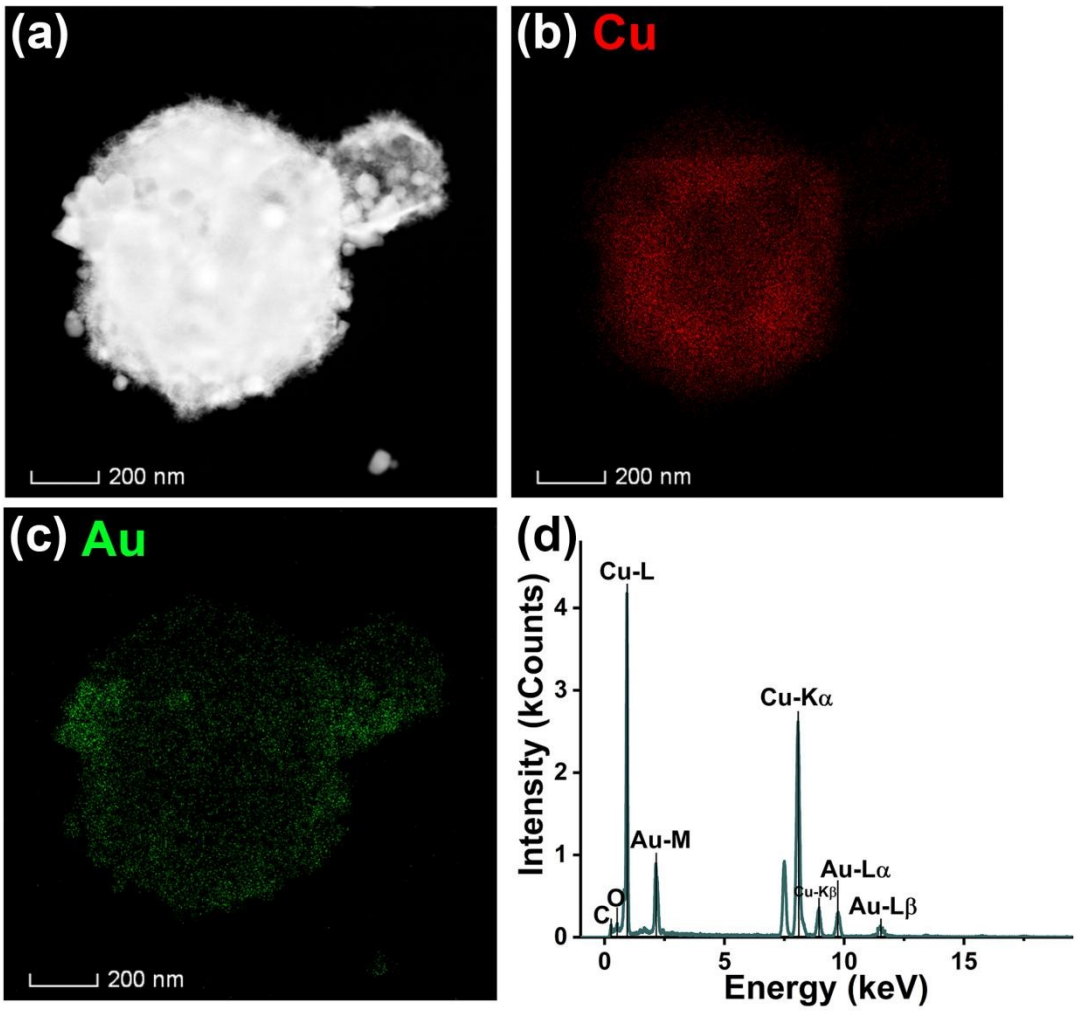

Figure S30. (a) NP-AuCu-1:5 morphology features in the HAADF-STEM image. EDS elemental mapping of NP-AuCu-1:5, indicating (b) Cu and (c) Au , and (d) the corresponding elemental spectrum. The Au:Cu atomic ratio of NP-AuCu-1:5 is 9:91.

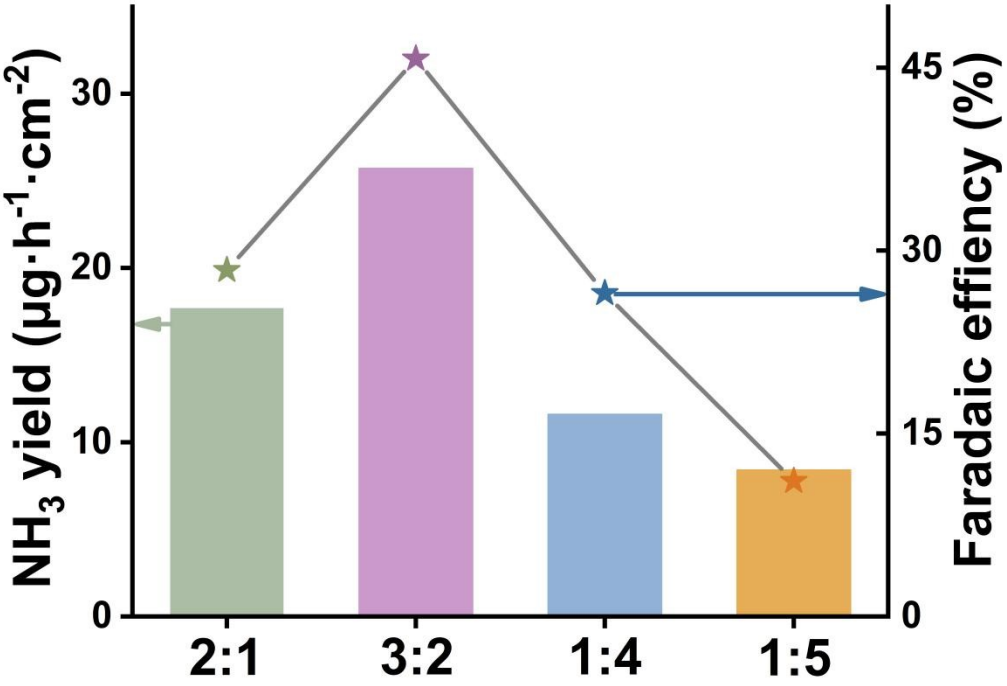

Figure S31. Faradaic efficiency at -0.80 V vs RHE and yield rate for ammonia at -0.95 V vs. RHE of NP-AuCu with different Au:Cu ratios in N_2 environment.

Table S1 Comparison of the ammonia yield and Faradaic efficiency for these different Au:Cu ratios.

Electrode Material	Au:Cu ratio	FE (%)	the ammonia yield ($\mu g \cdot h^{-1} \cdot cm^{-2}$)
NP-AuCu-2:1	76:24	28.4 ± 3.1	17.7 ± 2.7
NP-AuCu-3:2	**41:59**	**45.73 ± 2.1**	**25.72 ± 3.6**
NP-AuCu-1:4	14:86	26.5 ± 3.4	11.6 ± 3.0
NP-AuCu-1:5	9:91	11.1 ± 1.6	8.4 ± 1.7

Table S2 Comparison of the electrocatalytic NRR activities of AuCu alloy nanomaterials with other reported NRR catalysts under ambient conditions.

Electrode Material	electrolyte	FE(%)	NH_3 yield rate	Ref.
AuCu	**0.1 M Na_2SO_4**	**45.73**	**25.72 μg h^{-1} cm^{-2}**	**This work**
Ag_3Cu BPNs	0.1 M Na_2SO_4	13.28	9.84 μg h^{-1} cm^{-2}	1
a-Au/CeO_x–RGO	0.1 M HCl	10.10	8.3 μg h^{-1} mg^{-1}_{cat}	2
Au/TiO_2	0.1 M HCl	8.11	21.4 μg h^{-1} mg^{-1}_{cat}	3
NbO_2	0.05 M H_2SO_4	32	11.6 μg h^{-1} mg^{-1}_{cat}	4
pAu/NF	0.1 M Na_2SO_4	13.36	9.42 μg h^{-1} cm^{-2}	5
NPG@ZIF-8	0.1 M Na_2SO_4	44	(28.7±0.9) μg h^{-1} cm^{-2}	6
Cu/PI-300	0.1 M KOH	6.56	17.2 μg h^{-1} cm^{-2}	7
Au/CoO_x	0.05 M H_2SO_4	19	15.1 μg h^{-1} cm^{-2}	8
Pd_3Cu_1	1 M KOH	1.56	39.9 μg h^{-1} mg^{-1}_{cat}	9
Pt/Au@ZIF	0.1 M HCl	44.8±4.2	(161.9±16.7) μg h^{-1} mg^{-1}_{cat}	10
Au/o-CFP	0.1 M Na_2SO_4	31.1	40.6 μg h^{-1} cm^{-2}	11
NiSb	0.1 M HCl	48	56.9 μg h^{-1} cm^{-2}	12
THH Au NRs	0.1 M KOH	4.1	1.648 mg h^{-1} cm^{-2}	13
Rh-Mo_2C	0.05 M Na_2SO_4	15.4	26.3 μg h^{-1} cm^{-2}_{cat}	14
AuPdP NWs	0.1 M Na_2SO_4	15.44	7.51 μg h^{-1} cm^{-2}	15
AuNPs@MoS_2	0.1 M Na_2SO_4	9.7	5.65 μg h^{-1} mg^{-1}_{cat}	16
Cu_3P@NC	0.1 M Na_2SO_4	6.3	10.4 μg h^{-1} mg^{-1}_{cat}	17
AuPd NSs	0.1 M Na_2SO_4	15.9	19.6 μg h^{-1} mg^{-1}_{cat}	18
PCuPc/O-CNT	0.01 M H_2SO_4	26.8	12.3 μg h^{-1} cm^{-2}	19
AuHNCs/ITO	0.5 M $LiClO_4$	30.2	3.9 μg h^{-1} cm^{-2}	20

Section S4 References

[1] H. Yu, Z. Wang, D. Yang, X. Qian, Y. Xu, X. Li, H. Wang, L. Wang, *J. Mater. Chem. A*, 2019, **7**, 12526-12531.

[2] S.-J. Li, D. Bao, M.-M. Shi, B.-R.Wulan, J.-M. Yan, Q. Jiang, *Adv. Mater.*, 2017, **29**, 1700001.

[3] M.-M. Shi, D. Bao, B.-R. Wulan, Y.-H. Li, Y.-F. Zhang, J.-M. Yan, Q. Jiang, *Adv. Mater*., 2017, **29**, 1606550.

[4] L. Huang, J. Wu, P. Han, A. M. Al-Enizi, T. M. Almutairi, L. Zhang, G. Zheng, *Small Methods*, 2019, **3**, 1800386.

[5] H. Wang, H. Yu, Z. Wang, Y. Li, Y. Xu, X. Li, H. Xue, L. Wang, *Small*, 2019, **15**, 1804769.

[6] Y. Yang, S.-Q. Wang, H. Wen, T. Ye, J. Chen, C.-P. Li, M. Du, *Angew. Chem*. *Int. Ed*., 2019, **58**, 15362.

[7] Y.-X. Lin, S.-N. Zhang, Z.-H. Xue, J.-J. Zhang, H. Su, T.-J. Zhao, G.-Y. Zhai, X.-H. Li, M. Antonietti, J.-S. Chen, *Nat. Commun.*, 2019, **10**, 4380.

[8] J. Zheng, Y. Lyu, M. Qiao, J. P. Veder, R. D. Marco, J. Bradley, R. Wang, Y. Li, A. Huang, S. Jiang, S. Wang, *Angew. Chem. Int. Ed*., 2019, **58**, 18604.

[9] F. Pang, Z. Wang, K. Zhang, J. He, W. Zhang, C. Guo, Y. Ding, *Nano Energy*, 2019, **58**, 834-841.

[10] H. Y. F. Sim, J. R. T. Chen, C. S. L. Koh, H. K. Lee, X. Han, G. C. Phan-Quang, J. Y. Pang, C. L. Lay, S. Pedireddy, I. Y. Phang, E. K. L. Yeow, X. Y. Ling, *Angew. Chem. Int. Ed*., 2020, **59**, 16997-17003.

[11] J. Zhang, B. Zhao, W. Liang, G. Zhou, Z. Liang, Y. Wang, J. Qu, Y. Sun, L. Jiang, *Adv. Sci*., 2020, **7**, 2002630.

[12] G. Fan, W. Xu, J. Li, J.-L. Chen, M. Yu, Y. Ni, S. Zhu, X.-C. Su, F. Cheng, *Adv. Mater*., 2021, **33**, 2101126.

[13] D. Bao, Q. Zhang, F.-L. Meng, H.-X. Zhong, M.-M. Shi, Y. Zhang, J.-M. Yan, Q. Jiang, X.-B. Zhang, *Adv. Mater*., 2017, **29**, 1604799.

[14] B. Chang, H. Yuan, L. Li, J. Yu, X. Liu, W. Yu, B. Wang, L. Zhao, X. Liu, S.

Sun, H. Liu, W. Zhou, *Appl. Catal. B*-Environ., 2023, **320**, 121777.

[15] H. Wang, D. Yang, S. Liu, S. Yin, Y. Xu, X. Li, Z. Wang, L. Wang, *ACS Sustain. Chem. Eng.*, 2019, **7**, 15772-15777.

[16] Y. Zhou, X. Yu, X. Wang, C. Chen, S. Wang, J. Zhang, *Electrochim. Acta*, 2019, **317**, 34-41.

[17] J. Li, X. Lu, J. Huang, K. Guo, C. Xu, *Chem. Commun*., 2022, **58**, 2678-2681.

[18] S. Yin, S. Liu, H. Zhang, S. Jiao, Y. Xu, Z. Wang, X. Li, L. Wang, H. Wang, *ACS Appl. Mater. Interfaces*, 2021, **13**, 20233-20239.

[19] C. Jiang, H. Xue, T. Wang, J. He, *ChemCatChem*, 2023, **15**, e202201631.

[20] M. Nazemi, S. R. Panikkanvalappil, M. A. El-Sayed, *Nano Energy*, 2018, **49**, 316-323.